Letter

Observation of a magnetic phase transition in monolayer $NiPS_3$

Lili Hu,[1,2,*] Hao-Xin Wang,[3,*] Yuzhong Chen,[1] Kang Xu,[2] Ming-Rui Li,[3] Haiyun Liu,[1] Peng Gu,[1] Yubin Wang,[2] Mengdi Zhang,[1] Hong Yao,[3,2,†] and Qihua Xiong[1,2,4,5,‡]

[1]*Beijing Academy of Quantum Information Sciences, Beijing 100193, People's Republic of China*

[2]*State Key Laboratory of Low-Dimensional Quantum Physics and Department of Physics, Tsinghua University, Beijing 100084, People's Republic of China*

[3]*Institute for Advanced Study, Tsinghua University, Beijing 100084, People's Republic of China*

[4]*Frontier Science Center for Quantum Information, Beijing 100084, People's Republic of China*

[5]*Collaborative Innovation Center of Quantum Matter, Beijing 100084, People's Republic of China*

(Received 9 January 2023; revised 15 March 2023; accepted 31 May 2023; published 22 June 2023)

Monolayer magnet of *XY* type composes a pivotal part of the two-dimensional magnetism. As an important suspected *XY*-type antiferromagnet, whether 1*L* $NiPS_3$ exhibits magnetic order remains elusive. Herein by helicity-resolved Raman and ultrafast spectroscopy of $NiPS_3$ from bulk to monolayer, we find that 1*L* $NiPS_3$ is magnetically ordered with a Berezinskii-Kosterlitz-Thouless (BKT) transition at $T_{BKT} \approx 140$ K. We have also performed large-scale density-matrix renormalization-group calculations to verify the ground state zigzag antiferromagnetic order and Monte Carlo simulation to confirm the BKT-transition temperature in 1*L* $NiPS_3$. Our investigations establish 1*L* $NiPS_3$ to be an *XY* antiferromagnet with a relatively high-temperature BKT transition, providing an important platform for investigating complex couplings and topological excitations.

DOI: 10.1103/PhysRevB.107.L220407

Two-dimensional materials have provided an important platform for fundamental physics and unprecedented device functionalities, driven by various elementary excitations in the two-dimensional (2D) limit resulting from peculiar confinement behaviors and strong interactions [1]. Recently, considerable progress has been made in the emergent 2D magnetic materials [2,3]. According to the Mermin-Wagner theorem, long-range ferromagnetism and antiferromagnetism breaking the continuous global symmetry in the 2D isotropic Heisenberg model are expected to be forbidden at finite temperatures [4]. However, the single-ion anisotropy caused by spin-orbit coupling and the interaction between adjacent layers can facilitate the realization of 2D long-range magnetic orders. A variety of 2D magnetic materials have been experimentally verified recently, most of which are of Ising type [5,6] or Heisenberg type [7,8]. In addition, it is theoretically proved that there may exist a special topological BKT transition at finite temperatures in an *XY*-like 2D system, hallmarked by the transition from bound vortice-antivortice pairs into free vortices [9]. The BKT phase transition is found to have a tight correlation with superfluidity [10], Bose-Einstein condensation [11], and superconductivity [12]. Only in material systems fitted with the *XY* model (or *XXZ* model with weak interlayer interaction), BKT transition is possible to be observed experimentally.

Recently, important progress in the many-body exciton [13], magnon-phonon coupling [14,15], and magnon-based device [16] has been made in the field of 2D antiferromagnetic (AFM) materials. The intralayer AFM MPX_3 (M = Fe, Ni, Mn, and X = S, Se) family has attracted increasing attention due to their (quasi)2D AFM, rich spin dimensionalities, strong coupling between multidegrees of freedom, and potential applications in quantum information technology [17,18]. With varying transition metal M atoms among Fe, Ni, and Mn, the magnetism in MPX_3 behaves as Ising ($FePS_3$), *XY* ($NiPS_3$), and Heisenberg type ($MnPS_3$). While the bulk MPX_3 exhibit the C_{2h} point group symmetry, the point group of the monolayer is D_{3d}. $NiPS_3$ inherits the lattice structure of the MPX_3 family, where the intralayer Ni^{2+} ions form a honeycomb lattice [19,20], as schematically shown in Fig. 1(a). The Ni^{2+} ions with the same spin direction form the zigzag ferromagnetic (FM) chains parallel to the a axis and the FM chains are coupled in an AFM manner. At about 155 K, bulk $NiPS_3$ undergoes a phase transition from zigzag antiferromagnetism to paramagnetism. The temperature dependence of phonon splitting and linear dichroism suggested that zigzag antiferromagnetism exists only within the thickness ranging from bulk to bilayer, with the monolayer found magnetically disordered due to enhanced spin fluctuation [21,22]. Note that the phonon splitting due to symmetry lowering from D_{3d} to C_{2h} by zigzag AFM order has been observed in monolayer $CoPS_3$, a sister compound of monolayer $NiPS_3$, making the magnetic phase of monolayer $NiPS_3$ more intriguing [23]. Meanwhile, some theoretical studies have suggested that there exists a magnetic order in the monolayer $NiPS_3$ [24,25]. Even it is highly suspected that BKT transition exists in monolayer $NiPS_3$, no phase transition has ever been detected experimentally till now. Whether there is a magnetic order in the monolayer $NiPS_3$ and how to detect this ordering has become

*These authors contributed equally to this work.
†Corresponding author: yaohong@tsinghua.edu.cn
‡Corresponding author: qihua_xiong@tsinghua.edu.cn

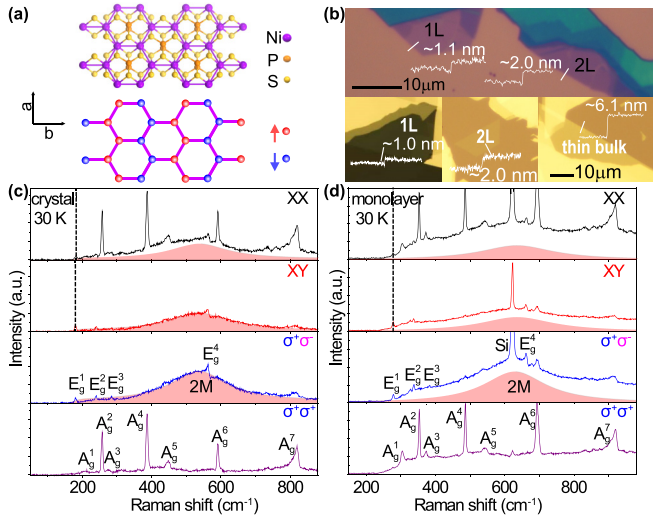

FIG. 1. The $NiPS_3$ samples and helicity resolved Raman spectra. (a) Lattice and magnetic structure of a single layer. (b) Optical photographs of monolayer and bilayer $NiPS_3$ for helicity-resolved Raman spectroscopy and monolayer, bilayer, and thin bulk $NiPS_3$ for ultrafast spectroscopy. The height of the samples is indicated by the atomic force microscopy cross section traces. (c), (d) Helicity-resolved Raman spectra of single crystal and monolayer at 30 K.

an urgent problem in the field of 2D magnetic materials. By determining critical exponent $\beta = 0.23$ even for bulk $NiPS_3$ [26], the *XY*-type spin dimensionality is confirmed in the system. Thus if a magnetic order exists in monolayer $NiPS_3$, it will be of BKT type. In addition, $NiPS_3$ has been regarded as a platform to study the intertwining physical phenomenon between spin and other degrees of freedom, which has not been fully understood [22]. Especially a spin-coupled coherent exciton has been observed in the $NiPS_3$ system which is very unusual for magnetic materials [13,22,27]. It was suggested that the disappearance of photoluminescence for the spin-correlated coherent exciton in monolayer can be attributed to the absence of magnetic order [13,22]. To understand *XY*-type antiferromagnetism and also to clarify the physical mechanism underlying the spin-coupled behaviors of charge, lattice, exciton, and magnon in the 2D limit towards rational manipulating these couplings, the experimental determination of magnetic order for $NiPS_3$ monolayer is highly demanded and critical. Here we report the experimental observation of robust magnetic order in monolayer $NiPS_3$. This conclusion is supported by results of helicity-resolved Raman and ultrafast spectroscopy, as well as by theoretical calculations. All our experimental observations and theoretical calculations support the magnetic phase transition at $\sim$140 K for monolayer $NiPS_3$. The details for sample preparation, spectra measurements, and theoretical calculations can be found in the Supplemental Material [28].

Figure 1(a) shows the schematic lattice structure and the magnetic order of a single layer $NiPS_3$ in the bulk systems. The upper panel of Fig. 1(b) shows the optical images of monolayer and bilayer $NiPS_3$ on Si/SiO_2 substrates for the purpose of helicity-resolved Raman spectroscopy measurements [30]. The three lower panels of Fig. 1(b) are the optical images of monolayer, bilayer, and thin bulk on transparent substrates (SiO_2 for monolayer, and sapphire for bilayer and thin bulk) used for the ultrafast spectroscopy experiments. The atomic force microscopy cross section traces are presented in Fig. 1(b) to characterize the sample thickness. The helicity-resolved Raman spectra of single crystal and monolayer $NiPS_3$ at 30 K are shown in Figs. 1(c) and 1(d), with the corresponding polarization configurations annotated, in which *XX* (*XY*) represents co- (cross-)linear polarization and $\sigma^+\sigma^+$ ($\sigma^+\sigma^-$) represent co- (cross-)circular polarization configurations, respectively. Note that the Raman background for monolayer is much higher than that for single crystal. The background is enhanced systematically along with the decrease of thickness as shown in Fig. S1 of the Supplemental Material [28]. The main phonon peaks are assigned in spectra under $\sigma^+\sigma^-$ and $\sigma^+\sigma^+$ polarizations to cover all the phonon peaks observed. As can be seen from Figs. 1(c) and 1(d), according to the polarization dependence observed, all the phonon peaks can be understood based on D_{3d} symmetry (see the Supplemental Material [28]), implying a weak interlayer interaction in the $NiPS_3$ system [31]. With the D_{3d} point group, the Raman active modes can be divided into A_g (out-of-plane vibration) and E_g (in-plane vibration) modes [32]. The frequency splitting of the spin-order sensitive E_g^1 mode under different linear polarizations (*XX* and *XY*) is denoted by the dashed lines in Fig. 1(c) and was utilized as a criterion to determine the existence of zigzag AFM order in $NiPS_3$ in a previous report [21]. Other than the narrow phonon peaks, there is a broad continuum scattering in Raman spectra as shown in Figs. 1(c) and 1(d), which is identified to be two-magnon scattering (denoted as the 2*M* mode) [21,33]. The 2*M* signal is highlighted by a red shadow, resulted from a composite line-shape analysis. It can be seen from Figs. 1(c) and 1(d) that the 2*M* band only appears in *XX*, *XY*, and $\sigma^+\sigma^-$ polarizations, while the scattering intensity under the $\sigma^+\sigma^-$ is about twice that under the *XY* polarization, indicating that the 2*M* modes belong to the E_g representation of the D_{3d} point group (see the Supplemental Material [28]). The existence of the 2*M* excitation itself does not guarantee the existence of magnetic order, since the 2*M* feature even exists at 290 K in paramagnetic bulk $NiPS_3$ as shown in Fig. S2(a) [28]. Note that the seeming spectra distortion at the low frequency tail is caused by the Raman filter as shown in Fig. S2.

The magnetic phase transition temperature can be determined by studying the temperature-dependent 2*M* excitation. To investigate these properties, the helicity resolved Raman spectroscopy is used. It should be noted that the nonhelicity resolved Raman spectroscopy including only *XX* and *XY* configurations was used to investigate the temperature evolution of phonons in Ref. [21]. The 2M scattering broadens at high temperatures, especially for $T > 150$ K, making it difficult to distinguish from the background in the spectra collected using *XY* polarization, as shown in Fig. S2. The use of $\sigma^+\sigma^-$ polarization can enhance the intensity of the 2*M* band and suppress the other complex signals. On the other hand, the 2*M* intensity detected at $\sigma^+\sigma^-$ doubles that at *XY* as shown in Fig. S2, indicating the persisting E_g symmetry of 2*M* at 290 K and further separating the 2*M* signal from the background. The 2*M* parameters at 290 K can be fitted well from $\sigma^+\sigma^-$ polarization geometry even for monolayer, as shown in

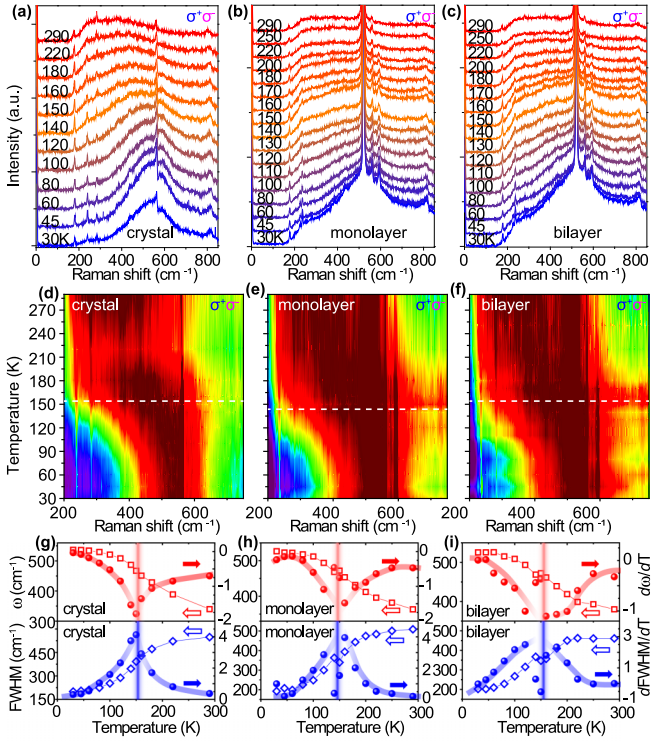

FIG. 2. Temperature-dependent Raman spectra of single crystal, bilayer, monolayer $NiPS_3$ at $\sigma^+\sigma^-$ polarization. (a)–(c) Temperature-dependent Raman spectra of single crystal, monolayer, and bilayer $NiPS_3$. (d)–(f) Color maps of normalized Raman spectra at $\sigma^+\sigma^-$ polarization for single crystal, monolayer, and bilayer $NiPS_3$. (g)–(i) Temperature dependence of frequency (ω), FWHM, $d\omega/dT$, and $d\mathrm{FWHM}/dT$ for single crystal, monolayer, and bilayer at $\sigma^+\sigma^-$ polarization.

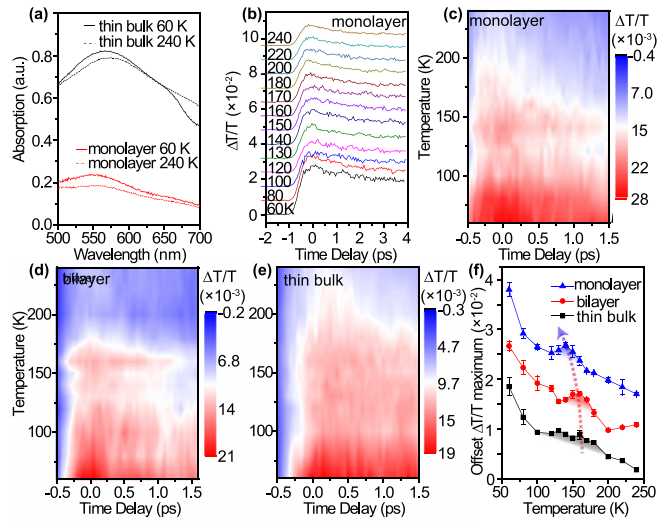

FIG. 3. Ultrafast spectroscopy investigation of $NiPS_3$. (a) The steady state absorption spectra of monolayer and thin bulk at 60 and 240 K. (b) The temperature-dependent ultrafast dynamics of monolayer $NiPS_3$. (c)–(e) The color map of time-resolved $\Delta T/T$ for monolayer, bilayer, and thin bulk $NiPS_3$. (f) The temperature dependence of $(\Delta T/T)_{\max}$ for monolayer, bilayer, and thin bulk.

Fig. S3. Because the 2M band has overwhelming intensity and a better signal-to-noise ratio under the $\sigma^+\sigma^-$ polarization, the 2M properties are mainly analyzed from Raman spectra at $\sigma^+\sigma^-$ polarization. Temperature-dependent Raman spectra of single crystals, monolayer, and bilayer (offset vertically for clarity) are shown in Figs. 2(a)–2(c) respectively. As the temperature increases from 30 to 290 K, the 2M band broadens and redshifts remarkably. Although the intensity decreases as temperature increases, the 2M band is still prominent even at 290 K. Across all the temperatures, the intensity at $\sigma^+\sigma^-$ polarization keeps almost twice that at XY polarization, obeying well the D_{3d} symmetry thus suggesting that in the whole temperature range the quasi-2D property of 2M can be maintained (see the Supplemental Material [28]). To further elaborate the temperature evolution of 2M bands, we normalize the Raman spectra to the maximum of the 2M band ($I_{2M}^{\max}$) under $\sigma^+\sigma^-$ polarization, and plot the normalized Raman spectra into color-map graphs, as shown in Figs. 2(d)–2(f). From the color maps, we can see that the frequency (ω) and full width at half maximum (FWHM) of 2M bands all show abrupt changes at $T \approx 150$ K for single crystal, monolayer, and bilayer. The values of ω and FWHM can be obtained by fitting the 2M band with a Lorentzian line shape. It is well known that the Néel temperature $T_N \approx 150$ K for bulk $NiPS_3$ corresponds to AFM-paramagnetic (PM) phase transition [22,24]. Thus the 2M properties indicate a magnetic phase transition for the $NiPS_3$ system of different thicknesses at about 150 K. We plot ω and FWHM of the 2M band with temperatures in Figs. 2(g)–2(i) to quantitatively analyze the temperature dependence of 2M properties, especially the remarkable change at magnetic phase transition temperature. The ω and FWHM are shown by the open squares and open diamonds in Figs. 2(g)–2(i). We also obtain the first-order derivatives of ω and FWHM versus temperature for single crystal, monolayer, and bilayer as shown by the red and blue balls in Figs. 2(g)–2(i), while the red and blue curves are guides for the eyes. The emergence of extremal points of $d\omega/dT$ and $d\mathrm{FWHM}/dT$ at ~140 K for monolayer strongly suggest that the monolayer $NiPS_3$ has magnetic ordering at low temperature.

We then investigate the transient absorption spectra of the monolayer, bilayer, and thin bulk $NiPS_3$ samples at variable temperatures, pumped by a 385-nm femtosecond laser pulse (see the Supplemental Material [28]). Figure 3(a) shows the steady-state absorption spectra of monolayer and thin bulk at 60 and 240 K, whose centers of the absorption peaks are about 570 and 560 nm, respectively, with a slight redshift with the increase of temperature. The wavelength chosen for analyzing the magnitude of the time-resolved $\Delta T/T$ is 532 nm to keep consistent with the Raman excitation wavelength (for other probe wavelengths, see the Supplemental Material [28]). Figure 3(b) shows the temperature-dependent ultrafast dynamics of monolayer $NiPS_3$ from 60 to 240 K, offset vertically for clarity. The color maps by plotting $\Delta T/T$ versus the time delays and the temperatures (60–240 K) are displayed in Figs. 3(c)–3(e) for monolayer, bilayer, and thin bulk respectively. As shown in Figs. 3(c) and 3(d), for the monolayer and bilayer, the magnitude of $\Delta T/T$ is decreasing with the increase of temperatures generally, but there is a local maximum near 150 K [31,32], which indicates that the phase

transitions of monolayer and bilayer $NiPS_3$ occur at about 150 K. For the thin bulk as shown in Fig. 3(e), the change of the color scale in 120–170 K is less sensitive to indicate the phase transition. We further extract the $(\Delta T/T)_{\max}$ of monolayer, bilayer, and thin bulk to plot versus the temperature in Fig. 3(f), vertically offset for clarity (the offset values are 5×10^{-3} for bilayer and 1×10^{-2} for monolayer). It can be seen that a plateaulike region of $(\Delta T/T)_{\max}$ appears at about 150 K for all samples, signifying the magnetic phase transition for monolayer, bilayer, and thin bulk $NiPS_3$, in accordance with the results of helicity-resolved Raman spectroscopy. The transition temperatures extracted from Fig. 3(f) are 160 K for bulk, 150 K for bilayer, and 140 K for monolayer. Since $NiPS_3$ is of *XY* type, with the thinning of the layers, it is likely that the phase transition changes from AFM-PM transition for the bulk to BKT transition for the monolayer.

To gain insight into the low-temperature magnetic phase, and the corresponding phase transition, we further perform theoretical calculations for the monolayer. DFT and classical Monte Carlo simulations have been conducted in Ref. [25], but these methods, which exclude the quantum fluctuation, in principle cannot generate a disordered state at low temperature. Also, the model they considered violates the monolayer D_{3d} symmetry since the parameters are determined by the measurement of the bulk $NiPS_3$. We consider a minimal effective spin-1 model on the honeycomb lattice including dominating spin-exchange coupling and single-ion anisotropy (SIA) which reads

$$H = J_1 \sum_{\langle i,\ j\rangle} \boldsymbol{S}_i \cdot \boldsymbol{S}_j + J_2 \sum_{\langle\langle i,\ j\rangle\rangle} \boldsymbol{S}_i \cdot \boldsymbol{S}_j + J_3 \sum_{\langle\langle\langle i,\ j\rangle\rangle\rangle} \boldsymbol{S}_i \cdot \boldsymbol{S}_j + D \sum_i \left(S_i^z\right)^2 ,$$

where $\langle i,\ j\rangle$, $\langle\langle i,\ j\rangle\rangle$, and $\langle\langle\langle i,\ j\rangle\rangle\rangle$ represent the nearest, the next-nearest, and the third-nearest neighbor (NN, NNN, and TNN) sites i and j, respectively. We adopt the following set of parameters according to DFT calculations [25]: $J_1 = -5.3$ meV, $J_2 = -0.2$ meV, $J_3 = 28$ meV, $D = 0.113$ meV. Here, anisotropy terms except single ion anisotropy (SIA) D are neglected after carefully considering the crystal field splitting of the Ni^{2+} ion and the crystal symmetry. Specifically, D is induced by spin-orbit-driven intermixing of the singlet ground state $3A_{2g}$ and the excited state $3T_{2g}$ [26,34], while other SIA terms are forbidden by the D_{3d} symmetry. The secondary anisotropy, the Dzyaloshinskii-Moriya exchange interaction, is forbidden by spin inversion symmetry between NN and TNN sites and is estimated to be smaller than 0.01 meV between NNN sites [35].

To investigate the low-temperature magnetic order of the J_1–J_2–J_3–D model, we implement a large-scale density matrix renormalization group (DMRG) calculation to find the ground state properties. The DMRG method is based on the ground state entanglement structure and can specifically capture the quantum fluctuation effects. We show the spin order in the ground state on a so-called XC6 cylinder in Figs. 4(a) and 4(b). The length of the red and blue arrows in Fig. 4(a) is proportional to the amplitude of the spin correlation $C(r, r_0) = \langle S^x_{r_0} S^x_r + S^y_{r_0} S^y_r \rangle$. Referred from a central site at r_0 [the purple cross in Fig. 4(a)], the in-plane spin

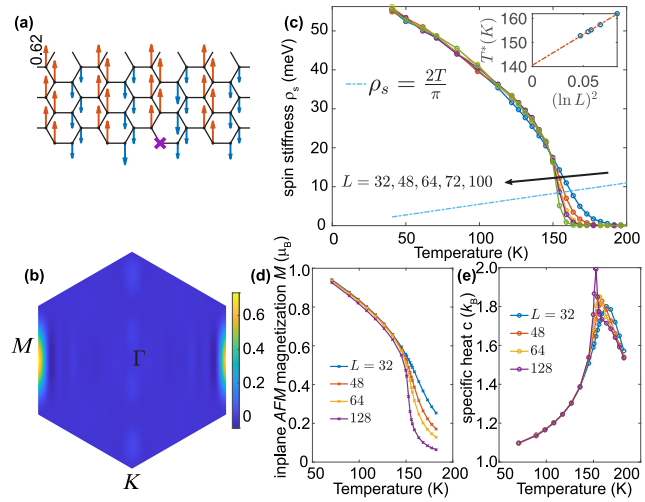

FIG. 4. Magnetic ground state and BKT transitions in monolayer $NiPS_3$. (a) In-plane spin correlations. (b) Sublattice spin structure factor for the ground state of the J_1–J_2–J_3–D model, calculated by DMRG. (c)–(e) Temperature dependence of the Monte Carlo computed spin stiffness, AFM magnetization, and specific heat at different linear size L.

correlation $C(r, r_0)$ shows a long-range zigzag AFM order with magnitude about 0.6, while the calculated z-component correlations are less than 0.1 and decay in power law, indicating an easy-plane spin orientation, i.e., monolayer $NiPS_3$ can be effectively described by the *XY*-type spin model. Figure 4(b) shows the sublattice spin structure factor $S_{AA}(q) = \frac{1}{L_1 L_2} \sum_{i\in A,\ j\in A} \langle S_i \cdot S_j \rangle e^{i\ q\cdot(r_i - r_j)}$. The sole peak around the M point as shown in Fig. 4(b) confirms the zigzag order at zero temperature and gives the value of the magnetic moment $m_s = 0.73$. In addition, we also explore the magnetic order on a different geometry YC6-cylinder which exhibits the same zigzag order (see the Supplemental Material [28]).

To justify the possibility of the BKT phase transition, we simulate the J_1–J_2–J_3–D model of classical spins based on the Monte Carlo method and determine the phase transition temperature by spin stiffness. The geometry in the simulation is torus with site number $L\times L\times 2$, where L is the linear size. The BKT transition can be determined by the temperature where an abrupt vanishing of the spin stiffness occurs. Figure 4(c) shows the results of stiffness for the different system sizes. Following the standard procedure of the finite-size extrapolation (see the Supplemental Material [28]), the transition temperature of monolayer $NiPS_3$ is estimated to be around 141 K, as shown in the inset to Fig. 4(c), in excellent agreement with the experimental result of 140 K. The calculated in-plane AFM magnetization and specific heat data plotted in Figs. 4(d) and 4(e) also support this transition temperature. We also find that the transition temperature is not sensitive to the magnitude of the SIA (see the Supplemental Material [28]).

As we have discussed above, the topological BKT phase transition offers an interpretation of the magnetic order in monolayer $NiPS_3$, namely, the quasi-long-range order formed below $T_{\rm BKT}$. This phase transition is characterized by the proliferation of topological defects, which are distinct from

magnons in the AFM background. The topological defects in zigzag AFM alignment can be understood as the vortices of the spin configuration of one of the zigzag sublattices. However, the previous experiments claim no magnetic order in monolayer $NiPS_3$ based on the absence of the frequency splitting between phonon peaks under *XX* and *XY* polarizations. Here, we propose two possible explanations that may resolve this contradiction. The first one is considering ubiquitous magnetic domains [25]. The three kinds of domains with different zigzag AFM directions related by C_3 rotational symmetry in the monolayer will average the linear dichroism effect. Thus, in the presence of magnetic domains the frequency splitting cannot be used to indicate the magnetic order in monolayer $NiPS_3$. The second possible explanation is considering high-order spin interactions. Such interactions will induce higher-order coupling terms between the three zigzag orders in the Landau-Ginzburg free energy and lead to a candidate new phase where the three zigzag orders coexist, similar to the 3-Q pair-density-wave phase [36]. The three-zigzag ordered phase preserves the C_3 rotational symmetry thus the zigzag-order sensitive frequency splitting and linear dichroism vanish. On the other hand, strong 2M scattering is one of the characteristic excitations in AFM materials [37]. The critical behavior of 2M frequency at T_N has been reported [38], due to the qualitative change of spin correlation at the magnetic phase transition temperature. Here in (monolayer) $NiPS_3$ systems, the (quasi-)long-range spin correlation at $T < T_N$ (T_{BKT}) is replaced by the short-range spin fluctuation at $T \geqslant T_N$ (T_{BKT}), leading to the redshift of 2M frequency at T_N (T_{BKT}), as observed in Fig. 2. In addition, the linewidth of the 2M band can also experience a sudden change nearing the temperature that spin-wave gap opens, i.e., T_N, or the temperature that bound vortice-antivortice pairs forms, i.e., T_{BKT}. With temperature increase, the enhancement of the thermal excitation and the spin fluctuation will provide more relaxation pathways to the 2M excitation at $T \geqslant T_N$ (T_{BKT}) [39]. As a result, the temperature dependence of intrinsic properties of the 2M mode in $NiPS_3$ manifests the magnetic phase transition effectively, i.e., both AFM-PM transition and BKT transition. In our work, the temperature-dependent frequency and FWHM of the 2M band confirm the existence of magnetic order for monolayer. Moreover, our analysis also unambiguously shows that the 2M Raman scattering, which mainly relies on the spin correlation, is a robust tool to study magnetic ordering in 2D magnetism. Since monolayer $NiPS_3$ is of *XY* type without interlayer interaction, it should be the BKT transition that happens in it.

In pump-probe transient spectroscopy, a phase transition can usually accompany the change of dielectric functions of materials, thus the time-resolved differential reflection ($\Delta R/R$) or transmission ($\Delta T/T$) can be used to detect the phase transition [40,41]. Usually the $\Delta R/R$ or $\Delta T/T$ is proportional to the excited carrier (or photoexcited quasiparticles) density. Since there is strong spin-charge coupling and spin-phonon coupling in $NiPS_3$ [21,42], the magnetic phase transition can change the dielectric function and thus the differential transmission $\Delta T/T$ can reflect the magnetic phase transition. When the $NiPS_3$ thickness changes from bulk to bilayer, it is therefore reasonable to assume that the pump induced excitation of a quasiparticle from the spin ground state to above the spin-wave gap will contribute to the differential $\Delta T/T$. As the temperature increases to near T_N, the spin-wave gap decreases and the high-energy phonons produced by carrier relaxation can excite the spin from the ground state to above the spin-wave gap, bringing an additional increase of $\Delta T/T$ at a temperature near T_N. This may be one of the important reasons why we can observe the magnetic phase transition in $NiPS_3$ from bulk to bilayer by ultrafast spectroscopy. In addition, in $NiPS_3$ monolayer of *XY* type the ultrafast dynamics can also be used to identify the quasi-long-range magnetic order. A recent theoretical investigation has pointed out that after a possible BKT phase transition in monolayer $NiPS_3$, the breaking of bound vortice-antivortice pairs into free vortices can contribute to the change of dielectric function across T_{BKT} [43], which can qualitatively explain the peak of $(\Delta T/T)_{max}$ that we observed in monolayer $NiPS_3$. Combining the results of 2M properties, the temperature dependent $(\Delta T/T)_{max}$ and the theoretical calculations, we can conclude that robust quasi-long-range magnetic order exists even in monolayer $NiPS_3$, whose magnetic phase transition should be of BKT type.

In summary, by studying the helicity-resolved Raman spectroscopy and the ultrafast spectroscopy with various thicknesses down to monolayer, we have unambiguously identified magnetic order in $NiPS_3$ from bulk to monolayer. By examining the 2M properties and transient absorptions, we obtained the phase transition temperatures of $NiPS_3$ with different thicknesses, which are about 160 K for bulk, 150 K for bilayer, and 140 K for monolayer, indicating AFM-PM phase transition in bulk and BKT transition in monolayer. Indeed, theoretical simulations show that monolayer $NiPS_3$ has zigzag AFM ordered ground state at zero temperature and BKT transition at finite temperatures. Therefore, our investigations convincingly settle that the monolayer $NiPS_3$ is a 2D *XY*-type antiferromagnet, providing a promising platform for topological excitations and magnetism engineering.

Q.X. gratefully acknowledges funding support from the National Natural Science Foundation of China (Grant No. 12020101003) and strong support from the State Key Laboratory of Low-Dimensional Quantum Physics at Tsinghua University. H.Y. gratefully acknowledges funding support from National Basic Research Program of China under Grant No. 2021YFA1400100.

[1] S. Z. Butler, S. M. Hollen, L. Cao, Y. Cui, J. A. Gupta, H. R. Gutiérrez, T. F. Heinz, S. S. Hong, J. Huang, A. F. Ismach *et al.*, ACS Nano **7**, 2898 (2013).

[2] C. Gong and X. Zhang, Science **363**, eaav4450 (2019).

[3] M. Gibertini, M. Koperski, A. F. Morpurgo, and K. S. Novoselov, Nat. Nanotechnol. **14**, 408 (2019).

[4] N. D. Mermin and H. Wagner, Phys. Rev. Lett. **17**, 1133 (1966).

[5] B. Huang, G. Clark, E. Navarro-Moratalla, D. R. Klein, R. Cheng, K. L. Seyler, D. Zhong, E. Schmidgall, M. A. McGuire, D. H. Cobden *et al.*, Nature (London) **546**, 270 (2017).

[6] X. Wang, K. Du, Y. Y. F. Liu, P. Hu, J. Zhang, Q. Zhang, M. H. S. Owen, X. Lu, C. K. Gan, P. Sengupta *et al.*, 2D Mater. **3**, 031009 (2016).

[7] C. Gong, L. Li, Z. Li, H. Ji, A. Stern, Y. Xia, T. Cao, W. Bao, C. Wang, Y. Wang *et al.*, Nature (London) **546**, 265 (2017).

[8] K.-Z. Du, X.-Z. Wang, Y. Liu, P. Hu, M. I. B. Utama, C. K. Gan, Q. Xiong, and C. Kloc, ACS Nano **10**, 1738 (2016).

[9] J. M. Kosterlitz and D. J. Thouless, J. Phys. C: Solid State Phys. **6**, 1181 (1973).

[10] P. Clade, C. Ryu, A. Ramanathan, K. Helmerson, and W. D. Phillips, Phys. Rev. Lett. **102**, 170401 (2009).

[11] T. P. Simula and P. B. Blakie, Phys. Rev. Lett. **96**, 020404 (2006).

[12] G. Blatter, M. V. Feigel'man, V. B. Geshkenbein, A. I. Larkin, and V. M. Vinokur, Rev. Mod. Phys. **66**, 1125 (1994).

[13] S. Kang, K. Kim, B. H. Kim, J. Kim, K. I. Sim, J.-U. Lee, S. Lee, K. Park, S. Yun, T. Kim *et al.*, Nature (London) **583**, 785 (2020).

[14] S. Liu, A. G. Del Águila, D. Bhowmick, C. K. Gan, T. Thu Ha Do, M. A. Prosnikov, D. Sedmidubský, Z. Sofer, P. C. M. Christianen, P. Sengupta, and Q. Xiong, Phys. Rev. Lett. **127**, 097401 (2021).

[15] L. Hu, K. Du, Y. Chen, Y. Zhai, X. Wang, and Q. Xiong, Natl. Sci. Open **2**, 20230002 (2023).

[16] G. Chen, S. Qi, J. Liu, D. Chen, J. Wang, S. Yan, Y. Zhang, S. Cao, M. Lu, S. Tian *et al.*, Nat. Commun. **12**, 6279 (2021).

[17] X. Jiang, Q. Liu, J. Xing, N. Liu, Y. Guo, Z. Liu, and J. Zhao, Appl. Phys. Rev. **8**, 031305 (2021).

[18] S. Rahman, J. F. Torres, A. R. Khan, and Y. Lu, ACS Nano **15**, 17175 (2021).

[19] M. A. Susner, M. Chyasnavichyus, M. A. McGuire, P. Ganesh, and P. Maksymovych, Adv. Mater. **29**, 1602852 (2017).

[20] M. Bernasconi, G. L. Marra, G. Benedek, L. Miglio, M. Jouanne, C. Julien, M. Scagliotti, and M. Balkanski, Phys. Rev. B **38**, 12089 (1988).

[21] K. Kim, S. Y. Lim, J.-U. Lee, S. Lee, T. Y. Kim, K. Park, G. S. Jeon, C.-H. Park, J.-G. Park, and H. Cheong, Nat. Commun. **10**, 345 (2019).

[22] K. Hwangbo, Q. Zhang, Q. Jiang, Y. Wang, J. Fonseca, C. Wang, G. M. Diederich, D. R. Gamelin, D. Xiao, J.-H. Chu *et al.*, Nat. Nanotechnol. **16**, 655 (2021).

[23] Q. Liu, L. Wang, Y. Fu, X. Zhang, L. Huang, H. Su, J. Lin, X. Chen, D. Yu, X. Cui *et al.*, Phys. Rev. B **103**, 235411 (2021).

[24] N. Sivadas, M. W. Daniels, R. H. Swendsen, S. Okamoto, and D. Xiao, Phys. Rev. B **91**, 235425 (2015).

[25] T. Y. Kim and C.-H. Park, Nano Lett. **21**, 10114 (2021).

[26] D. Afanasiev, J. R. Hortensius, M. Matthiesen, S. MañasValero, M. Šiškins, M. Lee, E. Lesne, H. S. van Der Zant, P. G. Steeneken, B. A. Ivanov *et al.*, Sci. Adv. **7**, eabf3096 (2021).

[27] X. Wang, J. Cao, Z. Lu, A. Cohen, H. Kitadai, T. Li, Q. Tan, M. Wilson, C. H. Lui, D. Smirnov *et al.*, Nat. Mater. **20**, 964 (2021).

[28] See Supplemental Material at http://link.aps.org/supplemental/10.1103/PhysRevB.107.L220407 for the details of the sample preparation and spectroscopy measurement; thickness dependent investigation of $NiPS_3$ at 30 K, with $\sigma^+\sigma^-$ polarization; helicity resolved Raman spectra for single crystal and monolayer $NiPS_3$ at 290 K; fitting of two-magnon band for monolayer $NiPS_3$ at 290 K; Raman tensor analysis; ultrafast spectroscopy with pump = 385 nm, probe = 510 and 560 nm; DMRG results of the J_1−J_2−J_3−D model on YC6 cylinder; single ion anisotropy dependence of the transition temperature. The Supplemental Material also contains Ref. [29].

[29] S. N. Neal, H.-S. Kim, K. R. O'Neal, A. V. Haglund, K. A. Smith, D. G. Mandrus, H. A. Bechtel, G. L. Carr, K. Haule, D. Vanderbilt, and J. L. Musfeldt, Phys. Rev. B **102**, 085408 (2020).

[30] S.-Y. Chen, C. Zheng, M. S. Fuhrer, and J. Yan, Nano Lett. **15**, 2526 (2015).

[31] D. Lançon, R. Ewings, T. Guidi, F. Formisano, and A. Wildes, Phys. Rev. B **98**, 134414 (2018).

[32] C.-T. Kuo, M. Neumann, K. Balamurugan, H. J. Park, S. Kang, H. W. Shiu, J. H. Kang, B. H. Hong, M. Han, T. W. Noh *et al.*, Sci. Rep. **6**, 20904 (2016).

[33] S. Rosenblum, A. H. Francis, and R. Merlin, Phys. Rev. B **49**, 4352 (1994).

[34] P. A. Joy and S. Vasudevan, Phys. Rev. B **46**, 5425 (1992).

[35] K. Yosida, D. C. Mattis, and K. Yosida, *Theory of Magnetism: Edition en Anglais* (Springer Science & Business Media, 1996), Vol. 122.

[36] H. Chen, H. Yang, B. Hu, Z. Zhao, J. Yuan, Y. Xing, G. Qian, Z. Huang, G. Li, Y. Ye *et al.*, Nature (London) **599**, 222 (2021).

[37] P. A. Fleury, J. Appl. Phys. **41**, 886 (1970).

[38] W. Brya and P. M. Richards, Phys. Rev. B **9**, 2244 (1974).

[39] H. Gretarsson, N. H. Sung, M. Höppner, B. J. Kim, B. Keimer, and M. Le Tacon, Phys. Rev. Lett. **116**, 136401 (2016).

[40] H. Chu, L. Zhao, A. de la Torre, T. Hogan, S. Wilson, and D. Hsieh, Nat. Mater. **16**, 200 (2017).

[41] Y. C. Tian, W. H. Zhang, F. S. Li, Y. L. Wu, Q. Wu, F. Sun, G. Y. Zhou, L. Wang, X. Ma, Q.-K. Xue, and J. Zhao, Phys. Rev. Lett. **116**, 107001 (2016).

[42] S. Y. Kim, T. Y. Kim, L. J. Sandilands, S. Sinn, M.-C. Lee, J. Son, S. Lee, K.-Y. Choi, W. Kim, B.-G. Park *et al.*, Phys. Rev. Lett. **120**, 136402 (2018).

[43] U. F. P. Seifert, M. Ye, and L. Balents, Phys. Rev. B **105**, 155138 (2022).